International Journal of Pharmaceutics 603 (2021) 120691

Contents lists available at ScienceDirect

International Journal of Pharmaceutics

journal homepage: www.elsevier.com/locate/ijpharm

Van der Waals force-driven indomethacin-ss-paclitaxel nanodrugs for reversing multidrug resistance and enhancing NSCLC therapy

Wenbo Kang, Yuanhui Ji *, Yu Cheng

Jiangsu Province Hi-Tech Key Laboratory for Biomedical Research, School of Chemistry and Chemical Engineering, Southeast University, Nanjing 211189, PR China

ARTICLE INFO

Keywords:
Self-assembled conjugates
Multidrug resistance-associated protein 1
Indomethacin
Paclitaxel
Nanomedicine

ABSTRACT

The high expression of multidrug resistance-associated protein 1 (MRP1) in cancer cells caused serious multidrug resistance (MDR), which limited the effectiveness of paclitaxel (PTX) in non-small cell lung cancer (NSCLC) chemotherapy. Indomethacin (IND), a kind of non-steroidal anti-inflammatory drugs (NSAIDs), which has been confirmed to be a potential MRP1 inhibitor. Taking into account the advantages of old drugs without extra controversial biosafety issue, in this manuscript, the disulfide bond (-S-S-) was employed for connecting IND and PTX to construct conjugate IND-S-S-PTX, which was further self-assembled and formed nanodrug (IND-S-S-PTX NPs). The particle size of IND-S-S-PTX NPs was ~160 nm with a narrow PDI value of 0.099, which distributed well in water and also exhibited a stable characteristic. Moreover, due to the existence of disulfide bond, the NPs were sensitive to the high level of glutathione (GSH) in tumor microenvironment. Molecular dynamics (MD) simulation presented the process of self-assembly in detail. Density functional theory (DFT) calculations revealed that the main driving force in self-assembly process was originated from the van der waals force. In addition, this carrier-free nano drug delivery systems (nDDs) could reverse the MDR by downregulating the expression of MRP1 protein in A549/taxol.

1. Introduction

Cancer has been regarded as an urgent public health issue worldwide. In America, lung cancer was responsible for a quarter of cancer deaths and had the highest estimated mortality rate in 2020. Meanwhile, the 5-year relative survival rate of lung cancer was barely 19%, which is just higher than that of pancreatic cancer (Siegel et al., 2020). Unfortunately, the typical type of lung cancer belongs to NSCLC, accounting for almost 85% (Duan et al., 2019). First-line chemotherapy was still the priority choice for NSCLC treatment (NSCLC Meta-analysis Collaborative Group, 2014). Paclitaxel (PTX), a tubulin inhibitor with excellent anti-tumor potential, which has been applied to some cancer therapies (such as breast cancer (Diéras et al., 2020; Tolaney et al., 2015), lung cancer (Herbst et al., 2018), etc.). However, poor aqueous solubility and multidrug resistance (MDR) limited its clinical application and chemotherapeutic efficacy (Szakacs et al., 2014). In addition, there are non-negligible side effects including peripheral neuropathy (Hertz et al., 2018), cardiotoxicity (Herrmann, 2020), nephrotoxicity (Mitin et al., 2013), serious hemolysis effect (Namgung et al., 2014), etc. Formed by high-pressure homogenization, Albumin-bound paclitaxel (Abraxane®, approved by FDA), with a mean diameter of 130 nm, has shown superb therapeutic index and greater rapid clearance than solvent-based (*sb*-) paclitaxel (Yardley, 2013). Encouraged by the promising performance of nano-scaled medicine, a variety of multifunctional, novel and greatly potential nano drug delivery systems (nDDs) has been constructed over the past few decades. Moreover, more and more nDDs have presented the characteristics of well-defined structure (Wang et al., 2016), high drug loading (Zhang et al., 2019), stimulating response to tumor microenvironment (Cheng and Ji, 2020; Wang et al., 2019a), controlled drug release (Jin et al., 2019; Zhen et al., 2018), prolonged blood circulation and synergistic treatment (Cheng et al., 2020; Yang et al., 2018). For example, inorganic nDDs - BP-DcF@sPL, which was based on black phosphorus, achieved the effect of chemotherapy (apoptosis/necrosis), photothermal therapy (local heat and reactive oxygen species (ROS) generation) and synergistic immunotherapy by increasing the secretion of interferon (IFN)-γ and promoting dendritic cell (DC) maturity (Ou et al., 2018). Ang-3I-NM@(siPLK1 + siVEGFR2), a kind of Polymeric nDDs, could overcome the blood–brain barrier and showed massive tumor accumulation and unique ROS responsiveness (Zheng et al., 2019). PTX-LH2(M) of peptide nDDs possessed cell penetrating

* Corresponding author.
E-mail address: yuanhui.ji@seu.edu.cn (Y. Ji).

https://doi.org/10.1016/j.ijpharm.2021.120691
Received 23 January 2021; Received in revised form 12 April 2021; Accepted 4 May 2021
Available online 7 May 2021
0378-5173/© 2021 Elsevier B.V. All rights reserved.

activity and showed great in-vivo efficacy (Nam et al., 2020). Clofarabine - Raltitrexed (CA:RT) of carrier-free nDDs exhibited a high drug loading, which obtained superior bioavailability, therapeutic effect and extremely reduced side effects in comparison to free drugs (Wang et al., 2018). In order to avoid the controversial biosafety issue of carrier materials, carrier-free nDDs was constructed for NSCLC therapy in this work, which possesses the nice performances of stability, appropriate solubility, sensitive release, well-defined structure and synergistic treatment.

Nano precipitation has been ubiquitous applied to prepare self-assembly nanoparticles (Xing et al., 2019). Even though many compounds or complicated materials have been reported to be successfully self-assembled into nanoparticles, it remained a great challenge for describing or explaining the mechanisms of self-assembly process in detail (Ianiro et al., 2019; Kim et al., 2017). However, molecular simulation could provide a unique angle to explore the mechanism of self-assembly process (Shao et al., 2020; Tavakkoli et al., 2016). Firstly, molecular dynamics (MD) simulations can visualize the self-assembly process in a vivid way by simplifying the model (Eslami et al., 2019b; Jain et al., 2019). Furthermore, non-bonding forces in the system, such as hydrogen bonding, electrostatic interactions, van der Waals forces and π-π stacking, can be captured dexterously, which has been widely regarded as driving forces in the self-assembly process (Chen et al., 2020; He et al., 2020; Shen et al., 2016; Wang et al., 2019b; Xiong et al., 2020; Zhang et al., 2020b). In addition, molecular simulation can also predict morphology of self-assembly micelle in specific ways (De Nicola et al., 2015; Li et al., 2019; Nie et al., 2015). More and more multiscale self-assembly process will be simulated properly and precisely with the development of algorithm model (Eslami et al., 2019a; Rolland et al., 2020; Wu et al., 2020). Therefore, for describing the self-assembly process of nDDs that we designed, MD simulations were utilized to visualize the formation of nanoparticles. The density functional calculations were employed to explore the driving forces.

A tricky problem for clinical chemotherapy of paclitaxel is inducing tumor immunosuppressive environment (TIME) (Chang et al., 2017). Furthermore, inflammation is often involved in the whole process (Palucka and Coussens, 2016). Paclitaxel can upregulate inflammatory ligands and receptors by activating toll-like receptor-4 (TLR4), which may cause systemic inflammation via inflammatory signaling pathways (NF-κB, PI3K, MAPK) (Ran, 2015; Volk-Draper et al., 2014). Hence, there are several inflammatory mediators over secretion such as tumor necrosis factor-α (TNF-α), vascular endothelial growth factor-A (VEGF-A), interleukin(IL)-1β, IL-6, IL-8 (Coussens et al., 2013; Nguyen et al., 2017; Shalapour and Karin, 2019). Those circulating inflammatory cytokines will promote the maturation, differentiation and recruitment of immunosuppressive cells (regulatory T cells (T_{reg}), myeloid-derived suppressor cells (MDSC), etc.), and further contribute to the TIME (Garner and de Visser, 2020). Multidrug resistance (MDR) is another obstacle which extremely restricts the clinical usage of PTX (Vaidyanathan et al., 2016). Multidrug resistance-associated protein 1 (MRP1), a kind of ABC transporter proteins, has tremendous ability to efflux massive anticancer drugs from cancer cells, which causes the low accumulation of anticancer drugs and the failing outcome of chemotherapy (Robey et al., 2018). Recently, immense evidence suggested that indomethacin (IND) not only applied to pain relief, fever recovery and anti-inflammatory but also could synergize antitumor activities. More importantly, IND was a great candidate for MRP1 inhibition (Lolli et al., 2019). Several in vivo models have confirmed that IND could down-regulate the expression of MRP1 protein and increase the intracellular accumulation of chemotherapy drugs (Lee et al., 2017; Zeng et al., 2020). Meanwhile, IND greatly improved efficacy on revising TIME and promoting immune response (Zhang et al., 2019). Extensive research has shown that IND can inhibit the synthesis of prostaglandin E2 and increase the polarization of M1 phenotype macrophages, which may help to rebalance the immunity and inhibit the tumor immune escape (Martinez-Colon and Moore, 2018). Therefore, indomethacin has excellent potential to diminish several intractable problems of PTX in clinical usage, and it contributes to synergetic NSCLCL therapy as a part of carrier-free nDDs that we constructed.

Considering the synergistic chemotherapy effect of IND, the superior toxicity towards tumor of PTX and the multifunctional feature of nDDs, novel carrier-free nDDs of indomethacin-S-S-paclitaxel (IND-S-S-PTX) was designed and synthesized, where PTX and IND were bridged by a disulfide bond. The prepared nanoparticles (NPs) could be sensitive to the tumor microenvironment of high expression of GSH and realized stimulus release. NPs also overcame the poor solubility of PTX and IND. MD simulation was employed to describe the self-assembly process of NPs in detail. Meanwhile, due to the downregulation of intracellular MRP1, A549/taxol showed more sensitivity towards IND-S-S-PTX NPs.

2. Materials and methods

2.1. Materials and reagent

N,N-dicyclohexylcarbodiimide (DCC), paclitaxel, dimethyl sulfoxide (DMSO), 4-dimethylaminopyridine (DMAP), indomethacin, 3,3′-dithiodipropionic acid and coumarin-6 were purchased from Tianjin Heowns Biochemical Technology Co., Ltd. (Tianjin, China). Methanol (CH_3OH), phosphate buffer saline (PBS, pH = 7.4), dichloromethane (DCM) and chloroform (TCM) were provided by Nanjing Wanqing Chemical Glass Ware & Instrument Co., Ltd. (Nanjing, China). Propidium iodide (PI), FITC-labeled Goat Anti-Rabbit IgG (H + L), MRP1/ABCC1 Rabbit Polyclonal Antibody, Annexin V-FITC, RPMI-1640 medium, A549 cells, fetal bovine serum and A549/taxol cells were offered by Beyotime Biotechnology Co., Ltd (Shanghai, China). The others analytically pure reagents were provided by commercial sources and could be utilized directly.

2.2. Synthesis of IND–SS–PTX conjugate

The synthetic routes were shown in Scheme 1. **Synthesis of IND-OH**: IND (5.0 g, 13.97 mmol), DCC (4.32 g, 20.937 mmol) and DMAP (0.17 g, 1.397 mmol) were respectively dissolved in DCM (25 mL) in the round-bottom flask. After stirring for 30 min at 0 °C, ethylene glycol (1.24 g, 16.755 mmol) was added drop by drop. The mixed system was further reacted under N_2 atmosphere at 0 °C. After 36 h, the crude product was extracted from mixed solution of DCM/water (ratio = 1:1) and subsequently purified by column chromatography method (eluent: CH_3OH/DCM = 1/80, V/V, silica gel) to obtain 3.3 g of pure IND-OH (yellow oil). The yield was 58%. ^{1}H NMR (600 MHz, DMSO) δ 7.67 (s, 2H), 7.64 (s, 2H), 7.05 (d, J = 2.5 Hz, 1H), 6.95 (d, J = 9.0 Hz, 1H), 6.72 (dd, J = 9.0, 2.6 Hz, 1H), 4.81 (s, 1H), 4.08 (d, J = 10.1 Hz, 2H), 3.78 (s, 2H), 3.77 (s, 3H), 3.60 – 3.56 (m, 2H), 2.22 (s, 3H). MS (ESI) m/z for $C_{21}H_{21}NClO_5$ $[M + Na]^+$: 424.0. **Synthesis of IND-COOH:**·10 mL TCM liquid contained DCC (1.337 g, 6.48 mmol) was added quite slowly to the mixed system of DMAP (60 mg, 0.49 mmol), 3,3′-dithiodipropionic acid (1.41 g, 6.71 mmol) and IND-OH (2 g, 4.986 mmol) under dry N_2. After stirring for 12 h, 20 mL TCM contained DCC (0.67 g, 3.24 mmol) was added and further heated to 65 °C. After refluxing for 3 h, crude product was poured into the separating funnel (500 mL) which contained the mixed solution of water and DCM (ratio: 1/1, V/V). Finally, column chromatography method was employed to gain the pure IND-COOH (eluent: CH_3OH/DCM = 1/40, V/V, silica gel). The yield was 83% (IND-COOH, yellow oil, 2.45 g). ^{1}H NMR (600 MHz, DMSO) δ 12.40 (s, 1H), 7.73 – 7.57 (m, 4H), 7.05 (d, J = 2.5 Hz, 1H), 6.94 (d, J = 9.0 Hz, 1H), 6.72 (d, J = 9.0 Hz, 1H), 4.27 (s, 4H), 3.78 (d, J = 12.7 Hz, 5H), 2.85 (dt, J = 9.7, 6.9 Hz, 4H), 2.67 – 2.55 (m, 4H), 2.23 (s, 3H). HRMS (ESI) for $C_{27}H_{28}ClNO_8S_2$ $[M + H]^+$: 594.10422. **Synthesis of IND-S-S-PTX**: DCC (0.725 g, 3.51 mmol) in 5 mL TCM solution was added to 30 mL DCM solution containing IND-COOH (2.34 g, 3.94 mmol), PTX (2.5 g, 2.93 mmol) and DMAP (35.8 mg, 0.293 mmol) under nitrogen protection. After stirring at 0 °C for 48 h, the crude product was acquired by

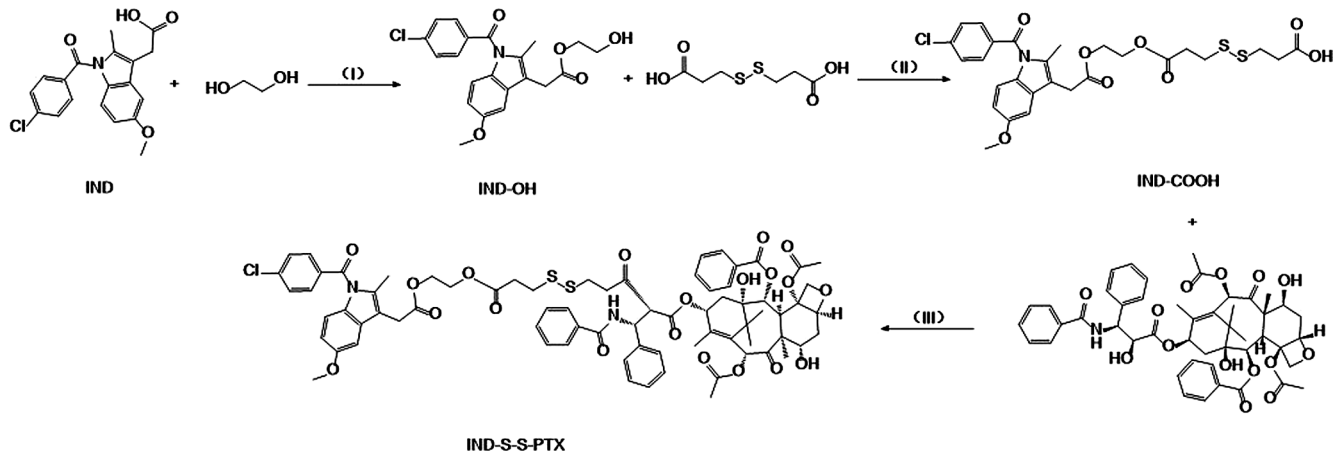

Scheme 1. Chemistry synthetic route of IND-S-S-PTX. Reagents and conditions: I) DCM, glycol, DCC, DMAP, IND, 0 °C, N_2, 36 h; II)DCC,DMAP, 3,3′-Dithiodipropionic, TCM, reflux, 12 h; III) PTX, DCC, DMAP, DCC, TCM, DCM, 0 °C, 48 h.

extracting from the mixed solution of DCM and water (ratio = 1:1). Then, column chromatography method (eluent: CH_3OH/DCM = 1/100, V/V, silica gel) was utilized to acquire 3.2 g pure IND-S-S-COOH (light yellow solid). The yield of reaction was 76.5%. ^{1}H NMR (600 MHz, DMSO) δ 9.19 (d, J = 8.6 Hz, 1H), 7.98 (d, J = 7.1 Hz, 2H), 7.84 (d, J = 7.1 Hz, 2H), 7.74 (t, J = 7.3 Hz, 1H), 7.69 – 7.61 (m, 6H), 7.54 (t, J = 6.1 Hz, 1H), 7.51 – 7.41 (m, 6H), 7.22 – 7.17 (m, 1H), 7.03 (d, J = 2.5 Hz, 1H), 6.93 (d, J = 9.0 Hz, 1H), 6.71 (dd, J = 9.0, 2.5 Hz, 1H), 6.29 (s, 1H), 5.83 (t, J = 8.7 Hz, 1H), 5.57 (s, 1H), 5.42 (d, J = 7.2 Hz, 1H), 5.37 (d, J = 8.8 Hz, 1H), 4.90 (d, J = 11.0 Hz, 2H), 4.63 (s, 1H), 4.26 (d, J = 3.2 Hz, 4H), 4.14 – 4.09 (m, 1H), 4.01 (dd, J = 16.5, 8.2 Hz, 2H), 3.77 (d, J = 16.6 Hz, 5H), 3.58 (d, J = 7.2 Hz, 1H), 2.88 (t, J = 6.9 Hz, 2H), 2.80 (dd, J = 14.1, 7.3 Hz, 4H), 2.57 (d, J = 13.9 Hz, 2H), 2.32 (t, J = 11.7 Hz, 1H), 2.23 (d, J = 15.8 Hz, 6H), 2.10 (s, 3H), 1.85 – 1.76 (m, 4H), 1.66 – 1.61 (m, 1H), 1.51 (d, J = 16.7 Hz, 4H), 1.01 (d, J = 17.9 Hz, 6H). HRMS (ESI) for $C_{74}H_{77}ClN_2O_{21}S_2$ $[M + Na]^+$: 1451.40844.

2.3. Preparation and characterization of IND-S-S-PTX NPs

IND-S-S-PTX NPs were formed by nano-precipitation method. In short, 1 mg IND-S-S-PTX was dissolved by 1.5 mL DMSO. Subsequently, the solution was added to 15 mL PBS drop by drop, stirring while adding. After 2 h, the mixed solution was placed into a dialysis bag (MW = 3.5 KDa) and subsequently dialyzed in deionized water for 48 h at 25 °C. Changing the water every 4 h and using 2 L deionized water for dialysis each time. Dynamic light scattering (DLS, Malvern Zetasizer Nano-ZS90, Malvern) was utilized to analyze the average size and the poly dispersity index (PDI) of nanoparticles in solution. The morphology of nanoparticles was observed by TEM (JEM-2100F, JEOL). Coumarin-6-loaded IND-S-S-PTX NPs were successful prepared (see Fig. S8) by using the same method of IND-S-S-PTX NPs.

2.4. Computational simulations

Molecular dynamics (MD) simulations and density functional theory (DFT) calculations were conducted to explore the self-assembly mechanism of IND-S-S-PTX NPs.

2.4.1. Molecular dynamics simulations

In this work, GAFF force field was used to describe IND-S-S-PTX and water, where the non-bond interaction was depicted by the coulomb potential and the Lennard-Jones (L-J) potential. The mixed L-J parameter was obtained from the Berthelot–Lorentz (L-B) mixing rule (Wang et al., 2004). Firstly, a cube box was constructed by packmol, which contained 10 IND-S-S-PTX molecules and 20,000 water molecules. In order to avoid overlapping of atomic coordinates, the energy of system was subsequently minimized to 10 KJ/mol by the steepest descent method. NVT MD simulation was utilized to simulate the operation for 20 ns to acquire a reasonable initial configuration. With further running 5 ns of NPT MD simulation, the system maintained the state of 300 K and 1.0 atm. Then, 15 ns of NPT MD simulation was performed again to obtain equilibrium. Another NPT MD simulation of 200 ns was conducted for data analysis with the trajectories stored every 1000 fs. In order to shorten the calculation time, SAHAKE method was hired to fix the bond between the system and H atom in the whole MD simulation process. The leap frog integrator was further employed to solve Newton's equations of motion with a time step of 2 fs, and periodic boundary conditions were used in the three-dimensional direction. For the non-bonding interactions in the mixed system, the cutoff distance was set as 1.4 nm, and the long-range electrostatic interaction was calculated by PME method. Meanwhile, Berendsen thermostat and Parrinello Rahman algorithm were utilized to control the temperature and pressure of the system. The coupling constants were 100 fs and 2000 fs respectively. All MD simulations were completed by GROMACS 5.1.4.

2.4.2. DFT calculations

DFT calculation was performed at M062X-D3/6-311G theoretical level to optimize the bimolecular IND-S-S-PTX and gain the binding energy, where D3 represented the Grimme's empirical dispersion correction (Zhang et al., 2020a). VMD was used to paint the molecular surface electrostatic potential. Gaussian 16 program package was employed to perform all the quantum mechanical calculations.

$$E_{Binding} = E_{AB} - E_A - E_B + \mathrm{BSSE} \quad (1)$$

E_{AB}: Counterpoise corrected energy; E_A: total energies of monomer A. E_B: total energies of monomer B; BSSE: basis set superposition error.

2.5. In vitro IND-S-S-PTX NPs release

The GSH-sensitively accumulative release of PTX and IND from IND-S-S-PTX NPs were conducted in the release medium of PBS (pH = 7.4) containing 10% FBS, with or without 10 mM GSH at 37.3 °C, under a shaking at the speed of 120 rpm/min. The dialysis bag (MW = 1000 Da) containing 1 mL solution of IND-S-S-PTX NPs was put into 250 mL release media. 1 mL release media was withdrawn and determined at the selected time. The high-performance liquid chromatography (HPLC, essential IC-16, Shimadzu) was applied to determine the content of PTX (mobile phase: methanol/acetonitrile/water = 5/7/8) or IND (mobile phase: methanol/0.05% phosphoric acid aqueous solution = 70/30, V/V). During the whole process, the UV detection was set at 227 nm or 320 nm, the flow rate was 1 mL/min and the temperature of C18 column was

35 °C.

2.6. Cell culture and uptake study

A549 and A549/taxol were cultured with RPMI-1640 medium at 37 °C in a humidified incubator consisted of 5% CO_2. The culture medium containing 1×10^5 U/L penicillin, 10% fetal bovine serum (FBS) and 100 mg/L streptomycin.

The cellular uptake of drugs was observed by confocal laser scanning microscope (CLSM). In order to make the IND-S-S-PTX NPs have fluorescence signal, we attempted to load coumarin-6 into IND-S-S-PTX NPs. The cell nuclei were stained by DAPI. During the whole process, in short, 2×10^4 A549 cells were seeded into 24-well plates and incubated for 24 h. The media was removed and the cells were cultured with coumarin-6 (1 μg/mL) loaded in 40 μM IND-S-S-PTX NPs. After 1 h, the cells were washed (PBS, 3 times), fixed (paraformaldehyde, 14%, 15 min), stained and ultimately observed by CLSM.

2.7. In vitro cytotoxicity measurement

The potential cytotoxicity of IND-S-S-PTX NPs, IND and PTX towards cancer cells were assessed by MTT method. Namely, 2×10^4 A549 and A549/taxol were respectively seeded into 96-well plates, cultured for 24 h and made the cells adhere to the wall. Then, cancer cells were incubated with IND, PTX and IND-S-S-PTX NPs under the concentrations of 0.125, 0.5, 2, 8 and 32 μM. After 24 h, the culture media was removed and cancer cells were washed by using PBS.20 μL PBS solutions with 5 mg/mL MTT reagent were added into each well, A549 or A549/taxol cells were further incubated for another 4 h. the medium was removed and 150 μL DMSO was added. The absorbance of solution was measured at 570 nm by SpectraMax M2e molecular devices before centrifuging for 10 min. The cell viability was eventually evaluated by the relative absorption ratio of treatment and control groups. IC_{50} values were obtained by GraphPad Prism software.

2.8. Cell apoptosis study

1×10^4 A549 and A549/taxol cells were seeded into 6-well plate and cultured at the same condition above. The cells were treated with IND-S-S-PTX NPs, IND and PTX at the concentrations of 40 μM. After 48 h, all the cancer cells were digested with trypsin and subsequently centrifuged for 10 min. Annexin V-FITC and PI were used to stain the cells for the further apoptosis analysis by FACScan flow cytometer.

2.9. Determination of MRP1 level

The expression of MRP1 in A549 and A549/taxol were estimated by immunofluorescence. The cancer cells were cultured and treated by using similar way above. Subsequently, A549 or A549/taxol cells were incubated with MRP1/ABCC1 Rabbit Polyclonal Antibody for 2 h. IgG (H + L) (FITC-labeled Goat Anti-Rabbit IgG (H + L)) was employed to treat the cells at 25 °C for 0.5 h. ImageJ.JS software was hired to quantify the level of MRP1 by the fluorescent intensity. Besides, the cells were photographed by CLSM.

2.10. Cell-cycle analysis

1×10^5 A549 and A549/taxol cells were seeded into 6-well plate and cultured overnight respectively. Then, the media was replaced and cells were cultured with 40 μM PTX, IND and IND-S-S-PTX NPs. The cells were collected, fixed (70% ethanol V/V, −20 °C, 12 h) and stained with PI (50 μg/mL, 30 min, 4 °C) for the further analysis of cell cycle distribution by flow cytometry.

2.11. ROS assay

The intracellular ROS level was determined by 2′,7′-dichlorodihydrofluorescein diacetate (DCFH-DA) kit. Briefly speaking, A549 and A549/taxol cells were cultured and treated under the similar method of cell apoptosis study while the dose of the drugs was 5 μM. The cells were washed (2 mL, 3 times, PBS), stained (0.5 mL, 20 μM, DCFH-DA) and cultured for another 1 h under the similar condition above. The cells were washed with PBS solution. Eventually, flow cytometer was hired to analysis intracellular ROS level by detecting the dichlorofluorescein.

2.12. Statistical analysis

All the experimental data are presented as mean ± SD. SPSS 22.0 software was utilized to determine the statistical significance.

3. Results

3.1. Synthesis of IND-S-S-PTX conjugate

In order to make the conjugated drug molecules sensitive to the tumor microenvironment (TME), bridging disulfide bond as linker might be an appropriate choice (Sun and Zhong, 2020). Owing to the active group (carboxyl group) of indomethacin, indomethacin glycol fragment was subsequently given, which was corresponded to IND-OH. Eventually, 3,3′-dithiodipropionic acid was inserted as responsive fragment, which linked two hydroxyl compounds (PTX and IND-OH) and generated IND-S-S-PTX. All the intermediates were confirmed by ^{1}H NMR and HRMS. The results were presented in Figs. S1–S6.

3.2. Characterization of IND-S-S-PTX NPs

IND-S-S-PTX NPs were prepared by nanoprecipitation which was universally employed to construct nanoparticles (Cheng et al., 2020). The mean diameter of IND-S-S-PTX NPs was measured by DLS as 157.4 ± 0.68 nm (Fig. 1A), which agreed with the results observed by the TEM micrograph as shown in Fig. 1B. Therefore, it was speculated that IND-S-S-PTX NPs could accumulate abundantly into the TME by enhancing permeation and retention (EPR) effect (Zhang and Ji, 2019). A narrow PDI value of 0.099 ± 0.01 indicated that IND-S-S-PTX NPs were well distributed in water. Moreover, it might keep stable in PBS containing 10% FBS under 4 °C (Fig. 1C). The critical micelle concentration of IND-S-S-PTX was 0.0539 mg/L as shown in Fig. 1D.

3.3. Self-assembly mechanism of nanoparticles

Here, MD simulations and DFT calculations were performed to analyze the mechanism of IND-S-S-PTX self-assembly process. Fig. 2 showed a dynamic snapshot of IND-S-S-PTX self-assembly process at different times. Firstly, 10 drug molecules were randomly dispersed into a cube containing 20,000 water by packmol. Initial equilibrium state of 0 ns was acquired by the 20 ns of NVT and NPT simulations. With the further performance of MD simulation, IND-S-S-PTX gradually gathered and eventually formed compact clusters at 200 ns. On the other hand, the solvent-accessible area gradually decreased to 84 nm^2, the average number of hydrogen bonds between IND-S-S-PTX and water decreased to 116, and the value of ΔG_{solv} was nearly increased to −100 kJ/(mol × nm^2) as shown in Fig. 3A and B, which indicated that IND-S-S-PTX spontaneously self-assembled into cluster in water.

It was difficult to form stable NPs from the single hydrophobic drugs by self-assembly process, while the modified amphiphilic drugs were much easier (Han et al., 2016). This might be due to the complex molecular interactions. Non-bonding interactions are always deemed as driving force in whole self-assembly process, for instance, van der Waals force, hydrogen bonding, π-π stacking, etc. To verify the driving force of self-assembly process, the interaction between molecules was further

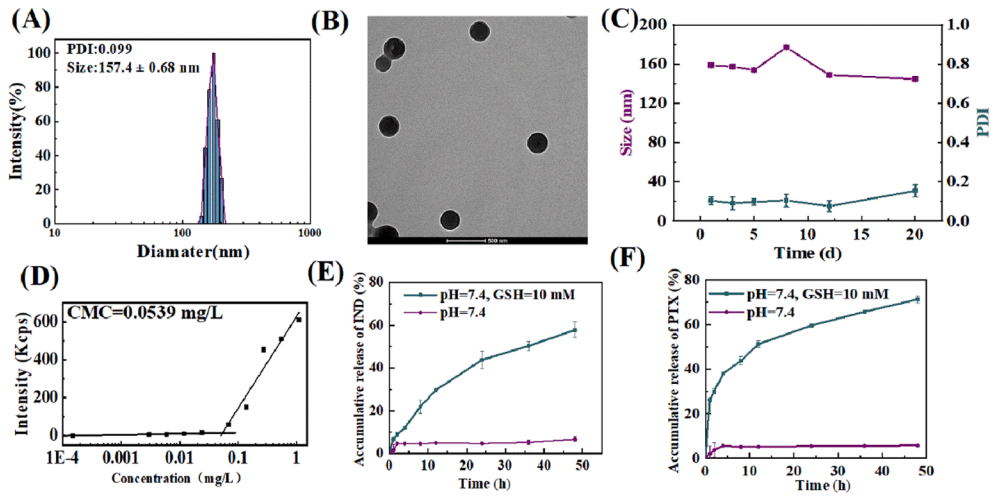

Fig. 1. (A) The size of IND-S-S-PTX NPs analyzed by DLS. (B) TEM image of IND-S-S-PTX NPs (C) The size change of IND-S-S-PTX NPs in PBS solution (pH = 7.4) containing 10% FBS, 4 °C. (D) The critical micelle concentration of IND-S-S-PTX. The in vitro release study of IND-S-S-PTX NPs. The GSH-sensitively accumulative release of IND (E) and PTX (F), under the condition of PBS with pH of 7.4 with or without 10 mM GSH.

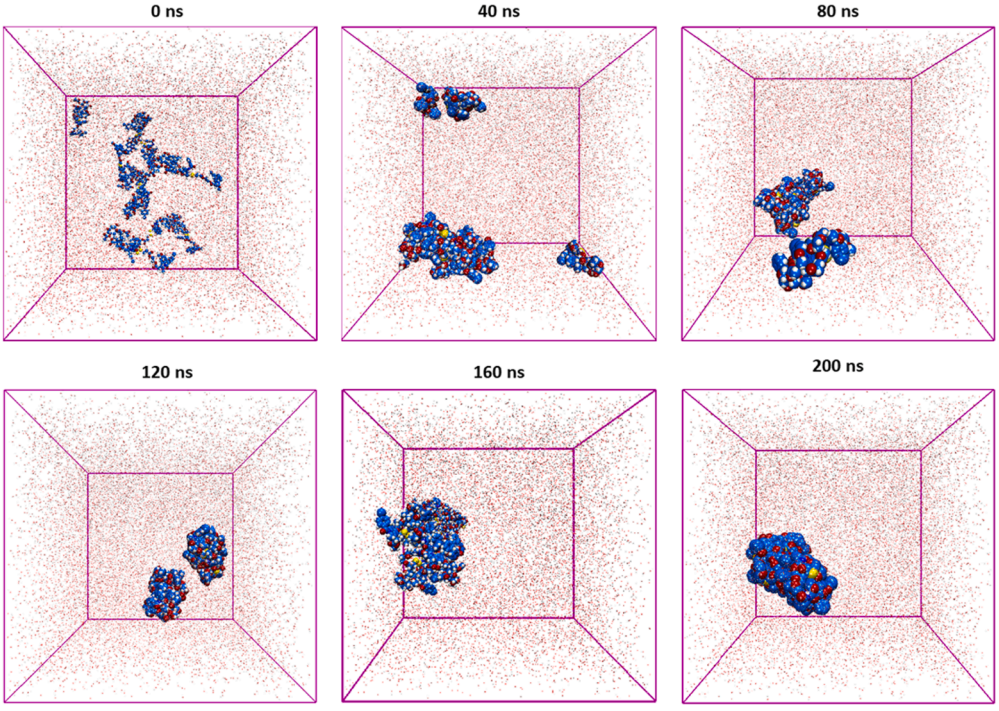

Fig. 2. Dynamic snapshot of IND-S-S-PTX self-assembly process.

detected by DFT calculation. Radial distribution functions (RDF) were able to provide the probability distribution of H_2O around IND-S-S-PTX (Zhang et al., 2020a). All oxygen atoms in IND-S-S-PTX and H atoms in H_2O were selected as reference sites to investigate the hydrogen bonds between IND-S-S-PTX and water. Fig. 3C and 3D showed that the first peak of O1-H RDF was extremely sharp and high. The value of peak height was 1.15 and the peak position was 1.78 Å, which meant the existence of hydrogen bond. Similarly, there were obvious hydrogen bonding interactions between O2, O3, O3, O4, O5, O6, O7, O8, O9, O10, O11 and water molecules. It was consequently speculated that there was strong hydrogen bond interaction between IND-S-S-PTX and water, which allowed the clusters to be dispersed well in water.

Electrostatic potential (ESP) analysis can adequately exhibit the characteristics of molecules, which is an effective means to predict non-covalent interactions. As observed in Fig. 4A, the aromatic ring region of IND-S-S-PTX had obvious negative electrostatic potential characteristics, while the hydroxyl group and carbonyl group containing lone pair electrons had obvious positive electrostatic potential characteristics. The extreme value of the electrostatic potential were +50.6 kJ/mol and −51.26 kJ/mol, respectively, which indicated IND-S-S-PTX molecules might produce strong non-bond interaction between IND-S-S-PTX and themselves. IGM analysis clarified that the non-bond interaction belonged to van der Waals force (Fig. 4B). The calculation of binding energy was −123.094 kJ/mol (Table S1), which confirmed that the van der Waals force was strong. The bimolecular structure was also selected for ESP analysis. It was found that the clusters formed by IND-S-S-PTX had non-bond interaction with water molecules too, which was agreed with the result of RDF analysis.

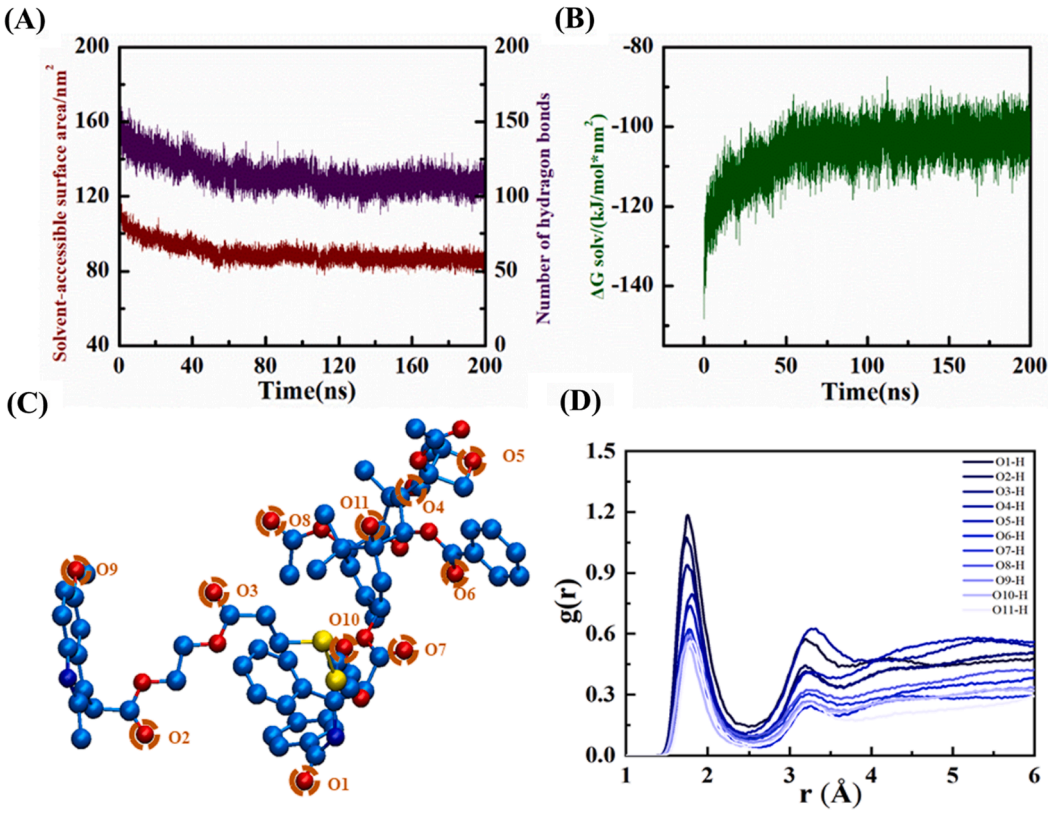

Fig. 3. (A) Solvent accessible surface area of IND-S-S-PTX cluster and the average number of hydrogen bonds between water and IND-S-S-PTX cluster. (B) Solvation free energy of IND-S-S-PTX nanostructures. (C) Oxygen atom diagram of RDF analysis. (D) RDF analysis of oxygen atom in IND-S-S-PTX.

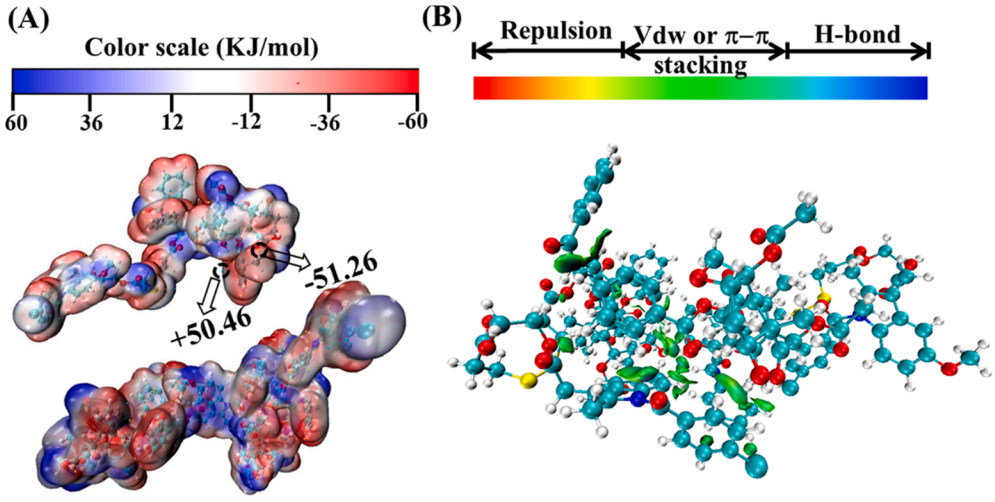

Fig. 4. (A) The ESP diagram of IND-S-S-PTX and bimolecular (B) Independent gradient model (IGM) analysis between IND-S-S-PTX and IND-S-S-PTX molecules.

3.4. *In vitro conjugate degradation and PTX release study*

It had been reported that the expression of GSH in TME was much higher than that in normal tissues, which allowed the selective release of IND-S-S-PTX NPs by the cleavage of the disulfide bond (Zhang and Ji, 2020). As shown in Fig. 1F, PTX was rapidly and massively released at the first 2 h under the condition of 10 mM GSH (PBS, pH = 7.4), while the IND was slow-released. Compared with the control group, the accumulative release of IND and PTX in 48 h were 57.8% and 71.3% respectively. However, less than 10% PTX and IND were released in a release medium without GSH. The result of the in-vitro release study approved the assumption that this carrier-free nDDs of IND-S-S-PTX could respond to the TME and this may be due to the degradation of disulfide bond (-S-S-) (Xue et al., 2016).

3.5. *Cellular uptake*

To demonstrate the cellular uptake of IND-S-S-PTX NPs, A549 and A549/taxol cells were respectively incubated with IND-S-S-PTX NPs, then further imaged by CLSM. Coumarin-6 was a great candidate to solve the shortcoming of IND-S-S-PTX NPs without inherent fluorescent signal (Xu et al., 2020). Here, coumarin-6-loaded IND-S-S-PTX NPs could present green fluorescent characteristics (Fig. 5). The cell nucleus was stained to blue by DAPI. As shown in Fig. 5A, coumarin-6-loaded

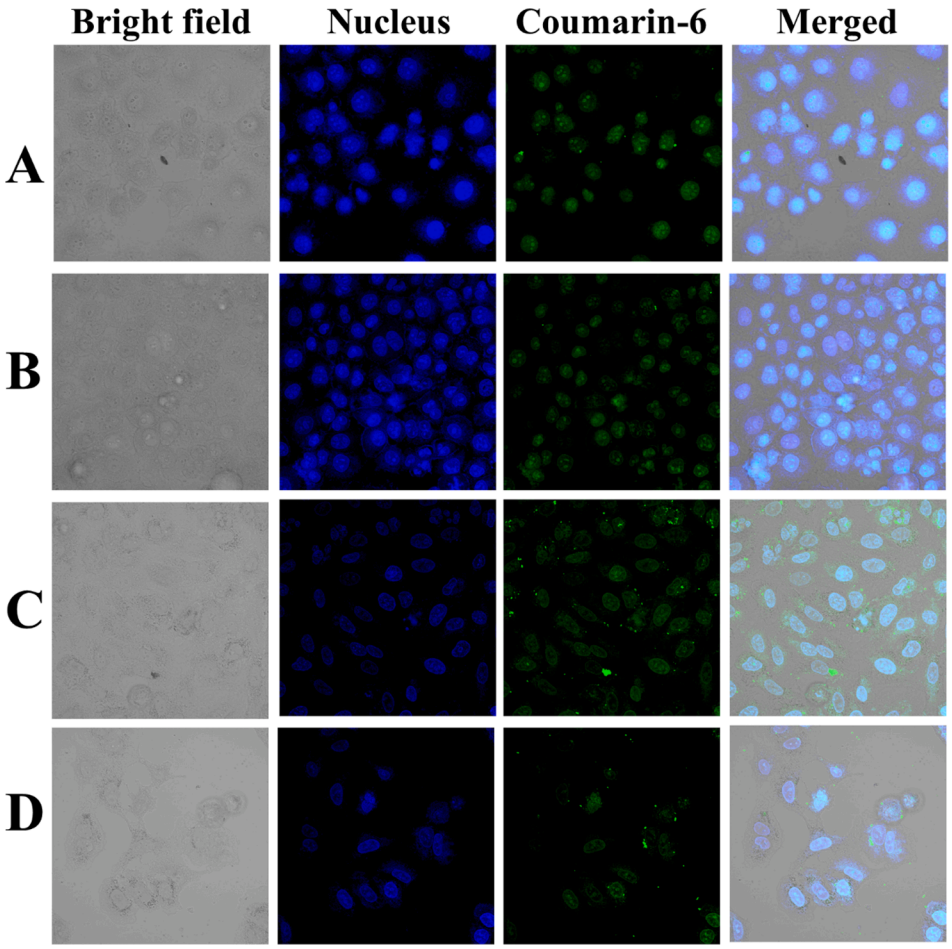

Fig. 5. Cellular uptake photos of coumarin-6 (1 μg/mL) loaded IND-S-S-PTX NPs by CLSM. (A) 1 h in A549 cells. (B) 3 h in A549 cells. (C) 1 h in A549/taxol cells. (D) 3 h in A549/taxol cells.

IND-S-S-PTX NPs could be quickly taken up by A549 in 1 h. Compared to Fig. 5B, there was no green fluorescent outside the A549 cells after 3 h. The same circumstances also appeared for A549/taxol, as exhibited in Fig. 5C and 5D. Therefore, it was observed that both A549 and A549/taxol could uptake IND-S-S-PTX NPs easily, smoothly and adequately.

3.6. *In vitro cytotoxicity assay*

In vitro cytotoxicity was a significant evaluation indicator for IND-S-S-PTX NPs, which reflected the potential antitumor effect. In order to figure out the bioactivity of IND-S-S-PTX NPs, MTT assay were conducted by using A549/taxol and A549 cells. IND and PTX were employed as positive controls. IC_{50} results were presented in Table 1 and Fig. 6. Compared to the results of antitumor effect, there was no obviously difference between PTX and IND-S-S-PTX NPs in A549 cells. The IC_{50} value of IND-S-S-PTX NPs was 10.247 ± 0.92 μM which just slightly higher than PTX but much lower than IND. While for the results in A549/taxol, the IC_{50} value of PTX was 29.871 ± 2.52 μM, which was nearly three times as high as that of IND-S-S-PTX NPs (10.791 ± 0.62 μM). Moreover, the IC_{50} value of IND-S-S-PTX NPs was close to half of IND (19.343 ± 1.67 μM). Hence, it was confirmed that IND-S-S-PTX NPs exhibited the most cytotoxicity and superior antitumor potential in A549/taxol, as observed in Table 1. Furthermore, the cell viability was decreased with the increased concentration of drugs. When the concentration of drugs was 8 μM, PTX and IND-S-S-PTX NPs showed the similar suppress cell proliferation in A549 (Fig. 6A). However, the results changed much in A549/taxol cells under the same concentration of drugs (Fig. 6B), IND-S-S-PTX NPs showed stronger ability in suppress cells proliferation, which consisted with the results of IC_{50} values. In vitro cytotoxicity assay verified that IND-S-S-PTX NPs showed outstanding potential in A549/taxol.

Table 1
Cytotoxicity of IND-S-S-PTX NPs, IND, and PTX towards A549 and A549/taxol.

Groups	IC50 values (μM)	
	A549	A549/taxol
IND-S-S-PTX NPs	10.247 ± 0.92	10.791 ± 0.62
IND	21.646 ± 1.92	19.343 ± 1.67
PTX	6.243 ± 0.45	29.871 ± 2.52

3.7. *Cell apoptosis study*

The cell apoptosis results were respectively presented in Figs. 7 and 8. The total apoptotic ratio of all groups in A549 were 49.4% (IND-S-S-PTX NPs), 21.49% (IND) and 65.5% (PTX). IND-S-S-PTX NPs was slightly inferior to PTX as shown in Fig. 7. However, in A549/taxol cells, IND-S-S-PTX NPs exhibited greater ability to induce apoptosis. The total apoptotic ratio of IND-S-S-PTX NPs was 49.0%, which was nearly 5 times as high as that of PTX (11.50%) and twice as high as that of IND (24.4%). Hence, it was obvious that IND-S-S-PTX NPs showed more sensitive to A549/taxol cells, which exhibited the feature of reversing multidrug resistance.

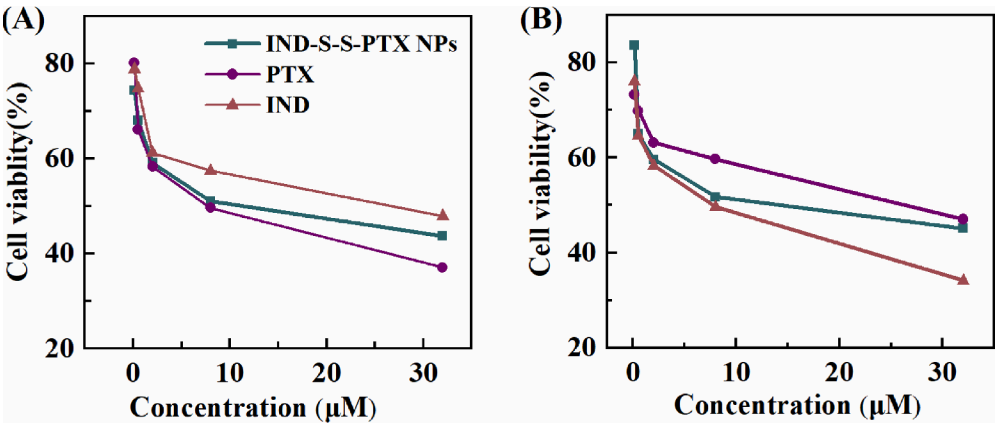

Fig. 6. Cell viability of (A) A549 or (B) A549/taxol after treated with IND-S-S-PTX NPs, IND and PTX in 24 h.

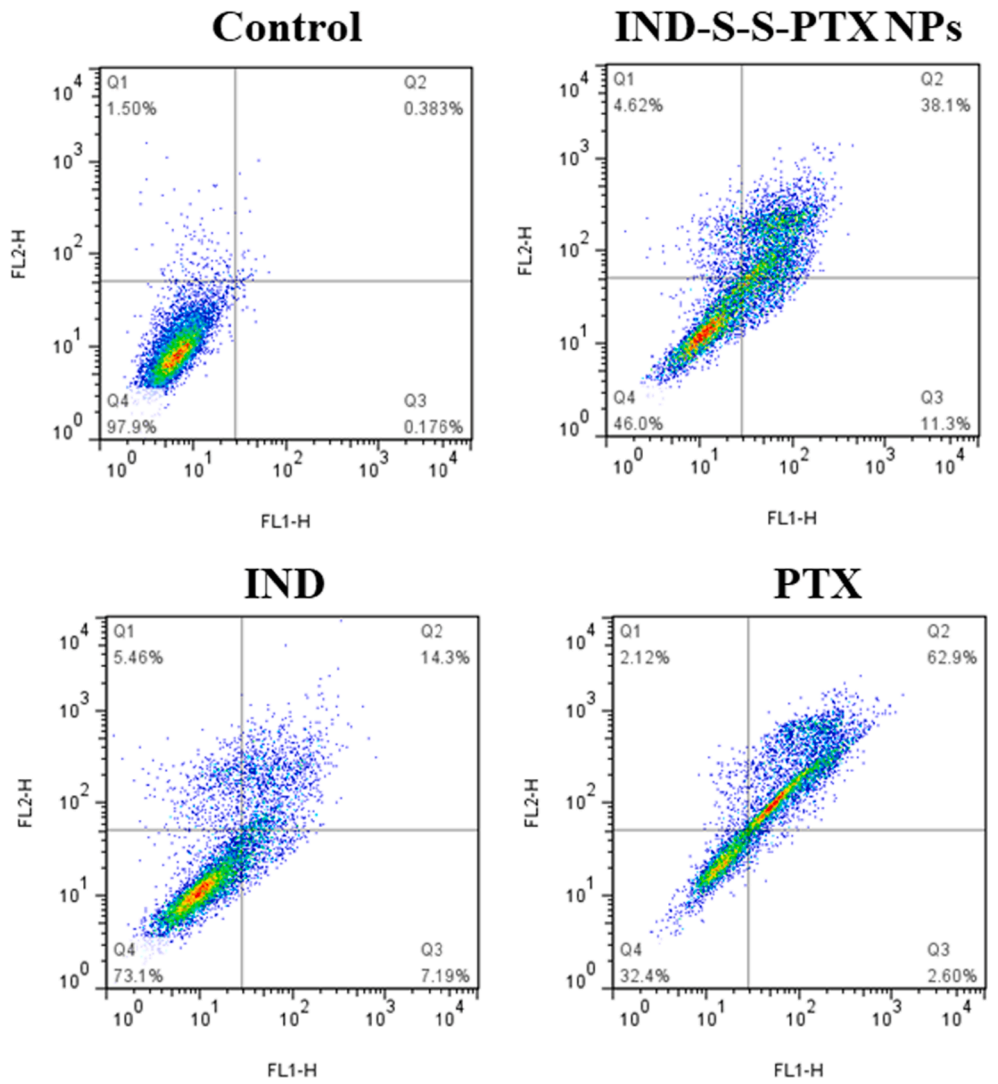

Fig. 7. Cell apoptosis study of IND-S-S-PTX NPs, IND, and PTX towards A549.

3.8. Cell-cycle analysis

In order to figure out the effect of IND-S-S-PTX NPs on cell cycle arrest, flow cytometry was implemented on A549 and A549/taxol cells. The results were shown in Fig. 9. As observed from Fig. 9, IND-S-S-PTX NPs might tend to arrest A549/taxol cells in S phase and G2/M phase. Compared to the control group, G0/G1 phase cells were decreased from 13.82% to 0, and G2/M phase cells also decreased from 36.82% to 28.35%. However, the S phase cells were greatly increased from 49.36% to 71.56%. In addition, the function mechanisms of IND-S-S-PTX NPs working on A549/taxol cells might be different from that of PTX. The percentage of cell cycle arrest in S phase was much higher than G2/M

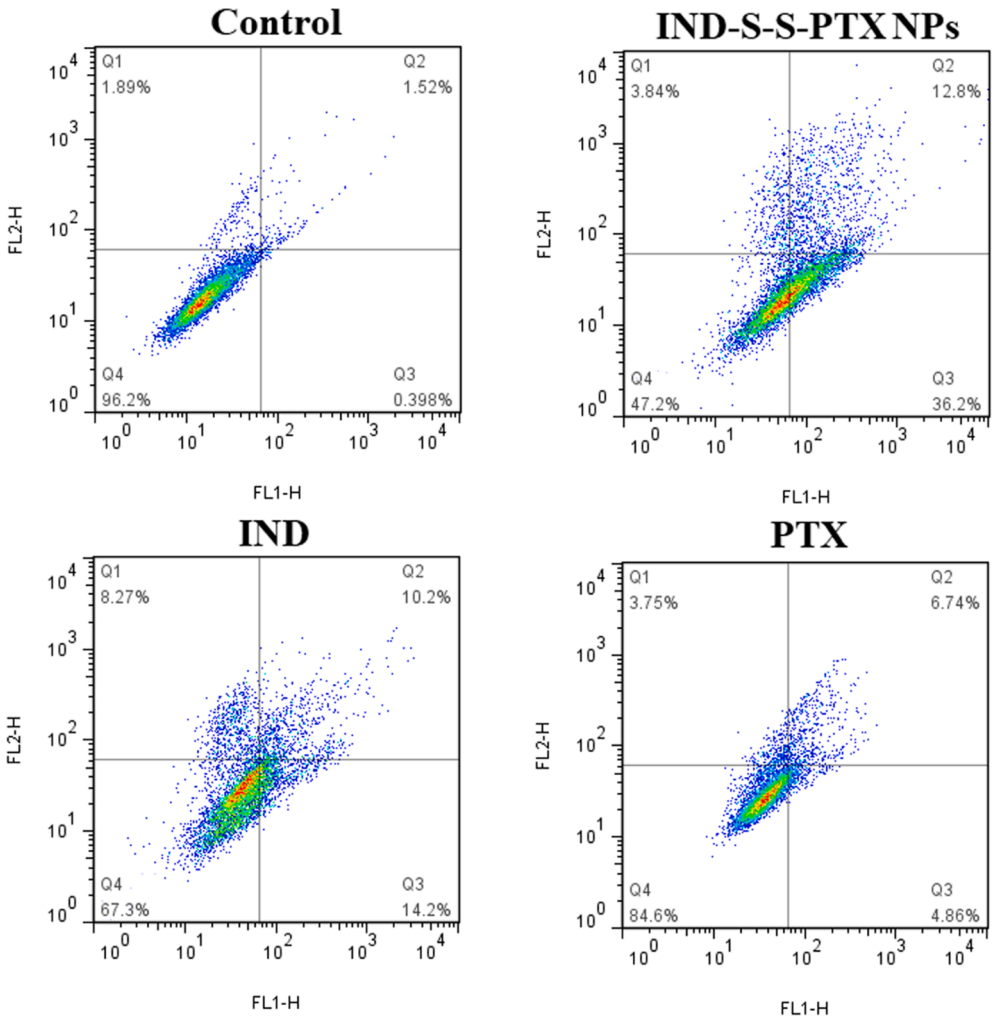

Fig. 8. A549/taxol apoptosis induced by IND-S-S-PTX NPs, IND, and PTX.

phase. The cell-cycle results of A549 were shown in Fig. S7.

3.9. MRP1 level determination

The overexpression of MRP1 protein was associated to MDR. IND had been proved to be an excellent MRP1 inhibition in A549/taxol cells. The MRP1 level was analyzed by the fluorescent intensity and the mean values were acquired from ImagineJ JS software. As shown in Fig. 10A, MRP1 protein was expressed in both A549 and A549/taxol, but more in A549/taxol. After treated with IND-S-S-PTX NPs, the expression of MRP1 was immediately decreased. The extent of reduction decreased significantly in A549/taxol cells. In order to observe the treatment effect intuitively, CLSM was employed. The results were presented in Fig. 10B and C. MRP1 protein was stained to green, while the nucleus was stained to blue. In A549/taxol, control group showed apparent green fluorescent sign, which meant the high level of MRP1. After incubated with IND-S-S-PTX NPs, the green fluorescent nearly disappeared (Fig. 10C). However, the PTX group remained strong green fluorescent. Hence, it was deduced that the down regulation of the expression of MRP1 in A549/taxol cells might be mainly responsible for excellent cell cytotoxicity and induced superior apoptosis of IND-S-S-PTX NPs.

3.10. ROS measurement

The intracellular ROS level of A549 and A549/taxol was detected by DCF-DA Kit. The results were displayed respectively in Figs. 11 and S6. Compared to control group, IND-S-S-PTX NPs could induce more ROS generation than other group in A549/taxol as observed in Fig. 11. Meanwhile, there were lower ROS level after treated with IND-S-S-PTX NPs than that treated with PTX group as found in Fig. S6. Therefore, combined with the performance of IND-S-S-PTX NPs in apoptosis and cytotoxicity assay, the high level of ROS might contribute to the induction of cell-cytotoxicity and apoptosis.

4. Discussions

Multidrug resistance limits the clinical usage of chemotherapy drug paclitaxel. A549/taxol expresses high level of MRP1 protein, which belongs to ABC transporters and associates closely with MDR (Stefan and Wiese, 2019). Paclitaxel is ingested by A549/taxol while MRP1 protein pumps it out, which causes the severe MDR. Nevertheless, the results of in vitro cytotoxicity assay and cell apoptosis study of A549 and A549/taxol exhibited different features. IND-S-S-PTX NPs were extremely sensitive to the A549/taxol and had excellent cytotoxicity and superior ability to induce apoptosis compared to paclitaxel. However, those advantages vanished in A549, the antitumor effect of IND-S-S-PTX NPs was nearly close to that of paclitaxel. This might be attributed to the following three main reasons. Firstly, compared to A549 cells, it maintained high level expression of MRP1 in A549/taxol cells. Under this circumstance, MDR might be the leading factor to restrict the therapy effect of paclitaxel. However, it was IND in IND-S-S-PTX NPs that could remarkably down regulate the expression of MRP1 in A549/taxol and

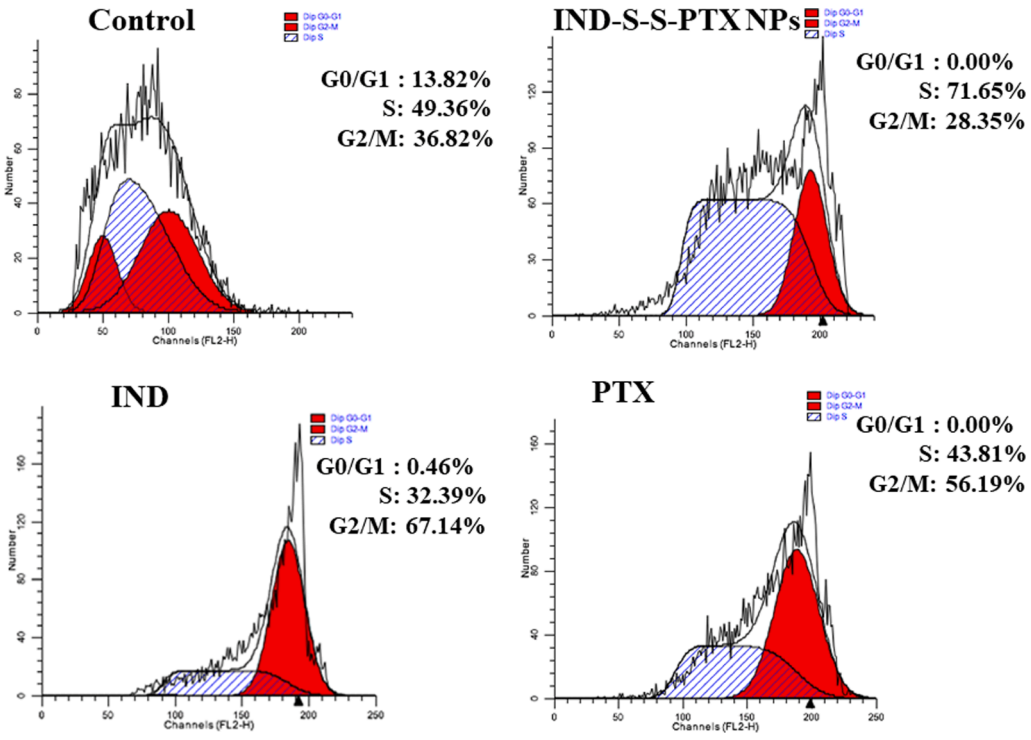

Fig. 9. The cell-cycle distribution of A549/taxol after incubating with IND-S-S-PTX NPs, IND, and PTX.

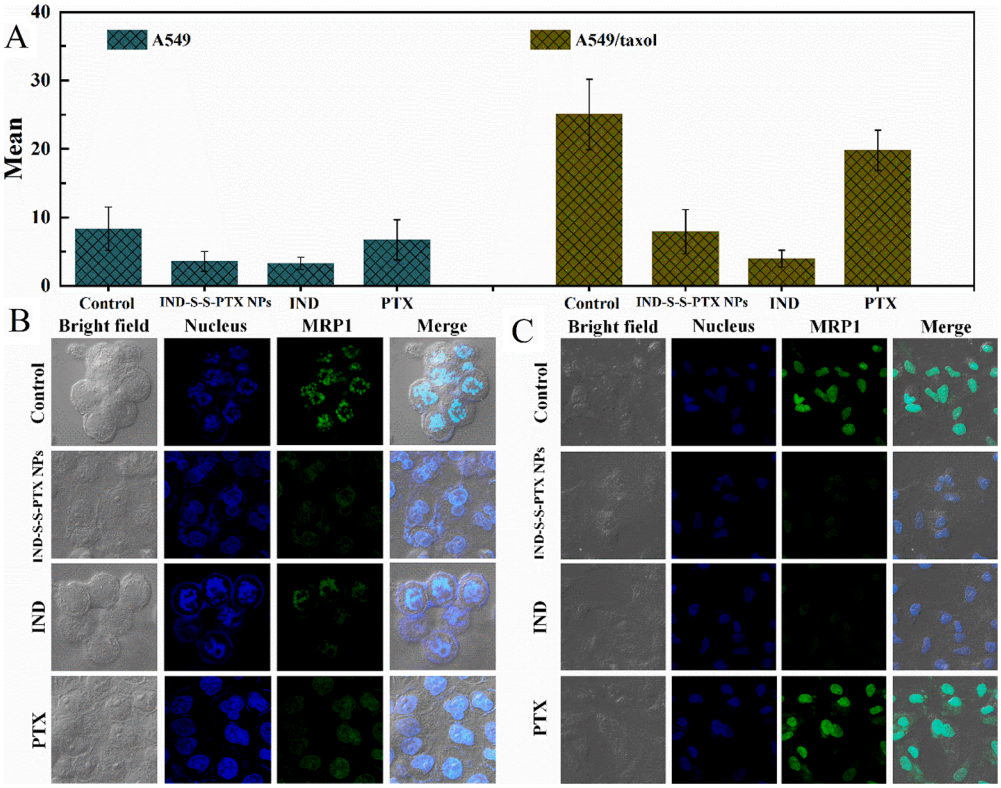

Fig. 10. (A) The mean immunofluorescence intensity of MRP1 in A549 or A549/taxol which was calculated by imagineJ JS. The expression of MRP1 in A549 (B) or A549/taxol (C) after treating with drugs imaged by CLSM.

reduce the paclitaxel outflow. Hence, the IC_{50} value of IND-S-S-PTX NPs was about a third of that of PTX and the apoptotic ratio of IND-S-S-PTX NPs was nearly 5 times as high as that of PTX. Moreover, in A549 cells, the high expression of MRP1 might not be the foremost obstacle for treatment. Although IND-S-S-PTX NPs could selectively respond to the TME with high level of GSH, the accumulated release ratio of PTX was only approximately 70% in 24 h, the low concentration of effective drugs might cause the antitumor effect of IND-S-S-PTX NPs barely the

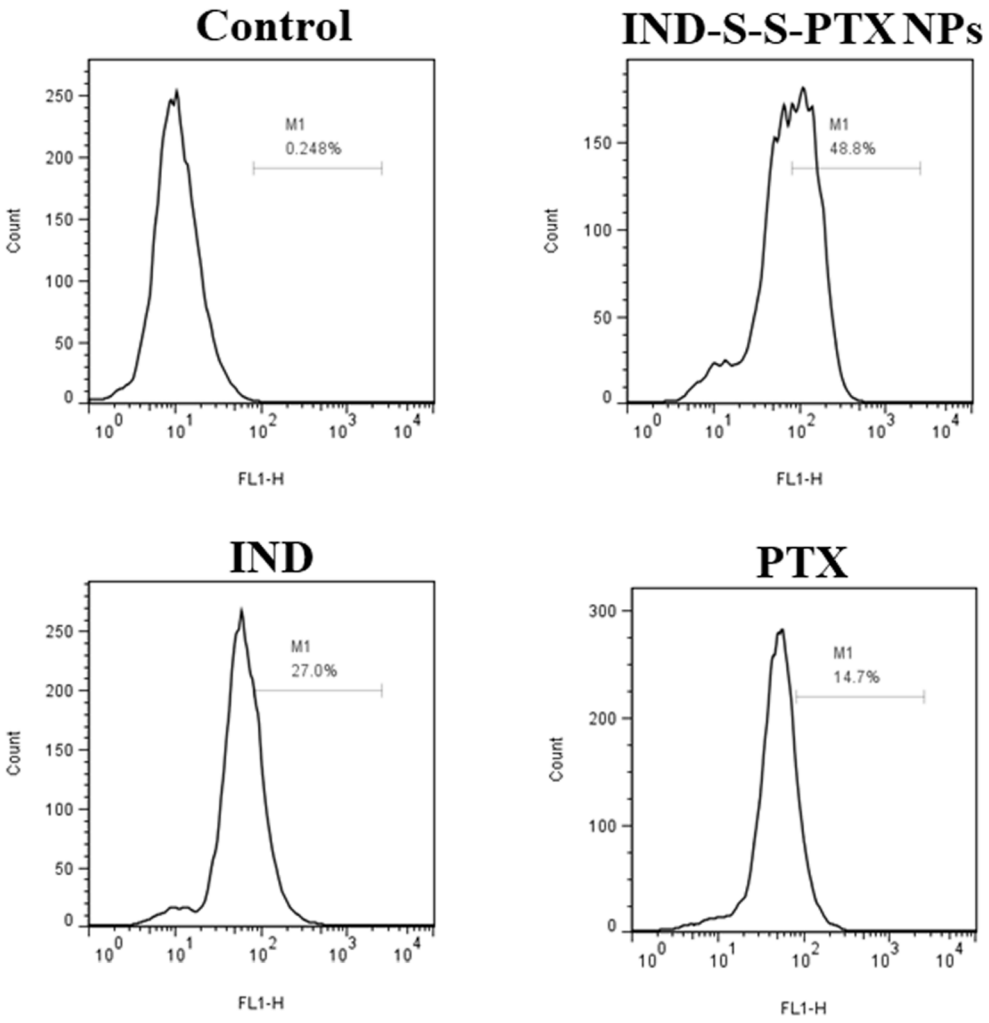

Fig. 11. Intracellular ROS level of A549/taxol measured by flow cytometry.

same level as PTX. Secondly, IND-S-S-PTX NPs could induce the more massive intracellular ROS generation in A549/taxol compared to that in A549 as observed the Figs. 11 and S6. It had been reported that the high level of ROS could contribute to the death of cancer cell, which was also the core strategy of photodynamic therapy (Teh et al., 2020). Finally, the cell-cycle interference mechanism of IND-S-S-PTX NPs was changed. A549 or A549/taxol cells after been incubated with IND-S-S-PTX NPs showed the characteristics of arresting the S and G2/M phase cells, especially for S phase cells. It was quite different from either IND or PTX.

Although the antitumor effect of IND-S-S-PTX NPs was similar to that of PTX in A549 cells, carrier-free nDDs in the form of aqueous solution could improve the solubility of PTX. In addition, IND-S-S-PTX NPs could sensitively respond to the TME with high-level GSH. The low accumulated release ratio of PTX might have promising performance in enhancing the drug circulation. The suitable size of nanoparticles also might realize the EPR effect. IND and PTX had been widely used in clinical therapy. Therefore, the carrier-free nDDs probably face few biosafety issues than other nDDs. All of those demonstrated a novel idea of reverse MDR in NCLS clinical therapy.

5. Conclusions

Through the above work, a carrier-free nDDs strategy for NSCLC therapy was demonstrated. This carrier-free nDDs only consisted of IND-S-S-PTX NPs aqueous solution which was prepared by nanoprecipitation method. IND-S-S-PTX NPs showed several unique characteristics: 1. Bridging disulfide bond as linker of IND and PTX endowed NPs with the function of redox-response to target the high-level GSH TME; 2. Nanoparticle was easily obtained and kept stable for at least 20 days. 3. The size distribution of NPs in aqueous solution was highly uniform with the narrow value of PDI, and greatly improved the solubility of PTX; 4. IND-S-S-PTX NPs could obviously reverse MDR by down regulating the expression of MRP1 protein; 5. IND-S-S-PTX NPs showed obvious cytotoxicity and ability to induce apoptosis towards A549/taxol, in addition to up regulating the generation of intracellular ROS. Furthermore, molecular simulation was employed to reveal the mechanisms of self-assembly of IND-S-S-PTX NPs. The results of classic DFT calculations, IGM analysis and ESP analysis revealed that the driving force of self-assembly process was mainly originated from van der Waals force. RDG and a series of molecular dynamics simulation analysis indicated the spontaneity of the self-assembly process.

CRediT authorship contribution statement

Wenbo Kang: Conceptualization, Methodology, Data curation, Writing - original draft. **Yuanhui Ji:** Supervision, Project administration, Writing - review & editing, Funding acquisition. **Yu Cheng:** Data curation.

Declaration of Competing Interest

The authors declare that they have no known competing financial

interests or personal relationships that could have appeared to influence the work reported in this paper.

Acknowledgements

The authors gratefully acknowledge Dr. Defang Ouyang from University of Macau for the help with quantum chemistry calculations by using the Gaussian 16 program package and the financial support for this research from the National Natural Science Foundation of China (Grant No.: 21978047, 21776046), the Fundamental Research Funds for the Central Universities (Grant No.: 2242020K40033), and the Six Talent Peaks Project in Jiangsu Province (Grant No. XCL-079).

Appendix A. Supplementary material

Supplementary data to this article can be found online at https://doi.org/10.1016/j.ijpharm.2021.120691.

References

Chang, Y.S., Jalgaonkar, S.P., Middleton, J.D., Hai, T., 2017. Stress-inducible gene Atf3 in the noncancer host cells contributes to chemotherapy-exacerbated breast cancer metastasis. Proc. Natl. Acad. Sci. USA 114, E7159–E7168.

Chen, Z., Liao, M., Zhang, L., Zhou, J., 2020. Molecular simulations on the hydration and underwater oleophobicity of zwitterionic self-assembled monolayers. AIChE J. https://doi.org/10.1002/aic.17103.

Cheng, Y., Ji, Y., 2020. Mitochondria-targeting nanomedicine self-assembled from GSH-responsive paclitaxel-ss-berberine conjugate for synergetic cancer treatment with enhanced cytotoxicity. J. Control. Release 318, 38–49.

Cheng, Y., Ji, Y., Tong, J., 2020. Triple stimuli-responsive supramolecular nanoassembly with mitochondrial targetability for chemophotothermal therapy. J. Control. Release 327, 35–49.

Coussens, L.M., Zitvogel, L., Palucka, A.K., 2013. Neutralizing tumor-promoting chronic inflammation: a magic bullet? Science 339, 286–291.

De Nicola, A., Kawakatsu, T., Rosano, C., Celino, M., Rocco, M., Milano, G., 2015. Self-assembly of triton X-100 in water solutions: a multiscale simulation study linking mesoscale to atomistic models. J. Chem. Theory Comput. 11, 4959–4971.

Diéras, V., Han, H.S., Kaufman, B., Wildiers, H., Friedlander, M., Ayoub, J.-P., Puhalla, S. L., Bondarenko, I., Campone, M., Jakobsen, E.H., Jalving, M., Oprean, C., Palácová, M., Park, Y.H., Shparyk, Y., Yañez, E., Khandelwal, N., Kundu, M.G., Dudley, M., Ratajczak, C.K., Maag, D., Arun, B.K., 2020. Veliparib with carboplatin and paclitaxel in BRCA-mutated advanced breast cancer (BROCADE3): a randomised, double-blind, placebo-controlled, phase 3 trial. Lancet Oncol. 21, 1269–1282.

Duan, F.-G., Wang, M.-F., Cao, Y.-B., Dan, L., Li, R.-Z., Fan, X.-X., Khan, I., Lai, H.-L., Zhang, Y.-Z., Hsiao, W.-W.-L., Yao, X.-J., Wu, Q.-B., Liu, L., Tang, Y.-J., Leung, E.-L.-H., 2019. MicroRNA-421 confers paclitaxel resistance by binding to the KEAP1 3′UTR and predicts poor survival in non-small cell lung cancer. Cell Death Dis. 10, 821.

Eslami, H., Khani, M., Muller-Plathe, F., 2019a. Gaussian Charge Distributions for Incorporation of Electrostatic Interactions in Dissipative Particle Dynamics: Application to Self-Assembly of Surfactants. J. Chem. Theory Comput. 15, 4197–4207.

Eslami, H., Khanjari, N., Muller-Plathe, F., 2019b. Self-Assembly Mechanisms of Triblock Janus Particles. J. Chem. Theory Comput. 15, 1345–1354.

Garner, H., de Visser, K.E., 2020. Immune crosstalk in cancer progression and metastatic spread: a complex conversation. Nat. Rev. Immunol. 20, 483–497.

Han, X., Chen, J., Jiang, M., Zhang, N., Na, K., Luo, C., Zhang, R., Sun, M., Lin, G., Zhang, R., Ma, Y., Liu, D., Wang, Y., 2016. Paclitaxel-Paclitaxel Prodrug Nanoassembly as a Versatile Nanoplatform for Combinational Cancer Therapy. ACS Appl. Mater. Interfaces 8, 33506–33513.

He, Y., Cong, C., Li, L., Luo, L., He, Y., Hao, Z., Gao, D., 2020. Sequential intra-intercellular delivery of nanomedicine for deep drug-resistant solid tumor penetration. ACS Appl. Mater. Interfaces 12, 8978–8988.

Herbst, R.S., Redman, M.W., Kim, E.S., Semrad, T.J., Bazhenova, L., Masters, G., Oettel, K., Guaglianone, P., Reynolds, C., Karnad, A., Arnold, S.M., Varella-Garcia, M., Moon, J., Mack, P.C., Blanke, C.D., Hirsch, F.R., Kelly, K., Gandara, D.R., 2018. Cetuximab plus carboplatin and paclitaxel with or without bevacizumab versus carboplatin and paclitaxel with or without bevacizumab in advanced NSCLC (SWOG S0819): a randomised, phase 3 study. Lancet Oncol. 19, 101–114.

Herrmann, J., 2020. Adverse cardiac effects of cancer therapies: cardiotoxicity and arrhythmia. Nat. Rev. Cardiol. 17, 474–502.

Hertz, D.L., Kidwell, K.M., Vangipuram, K., Li, F., Pai, M.P., Burness, M., Griggs, J.J., Schott, A.F., Van Poznak, C., Hayes, D.F., Lavoie Smith, E.M., Henry, N.L., 2018. Paclitaxel Plasma Concentration after the First Infusion Predicts Treatment-Limiting Peripheral Neuropathy. Clin. Cancer Res. 24, 3602–3610.

Ianiro, A., Wu, H., van Rijt, M.M.J., Vena, M.P., Keizer, A.D.A., Esteves, A.C.C., Tuinier, R., Friedrich, H., Sommerdijk, N., Patterson, J.P., 2019. Liquid-liquid phase separation during amphiphilic self-assembly. Nat. Chem. 11, 320–328.

Jain, A., Globisch, C., Verma, S., Peter, C., 2019. Coarse-Grained Simulations of Peptide Nanoparticle Formation: Role of Local Structure and Nonbonded Interactions. J. Chem. Theory Comput. 15, 1453–1462.

Jin, Z., Nguyen, K.T., Go, G., Kang, B., Min, H.K., Kim, S.J., Kim, Y., Li, H., Kim, C.S., Lee, S., Park, S., Kim, K.P., Huh, K.M., Song, J., Park, J.O., Choi, E., 2019. Multifunctional Nanorobot System for Active Therapeutic Delivery and Synergistic Chemo-photothermal Therapy. Nano Lett. 19, 8550–8564.

Wang, J., Wolf, M.R., Caldwell, W.J., Kollman, A.P., Case, A.D., 2004. Development and Testing of a General Amber Force Field. J. Comput. Chem. 25, 9.

Kim, J., Ou, Z., Jones, M.R., Song, X., Chen, Q., 2017. Imaging the polymerization of multivalent nanoparticles in solution. Nat. Commun. 8, 761.

Lee, J.Y., Termsarasab, U., Lee, M.Y., Kim, D.H., Lee, S.Y., Kim, J.S., Cho, H.J., Kim, D.D., 2017. Chemosensitizing indomethacin-conjugated chitosan oligosaccharide nanoparticles for tumor-targeted drug delivery. Acta Biomater. 57, 262–273.

Li, S., Xu, Q., Li, K., Wang, Y., Yu, C., Zhou, Y., 2019. Multigeometry Nanoparticles from the Orthogonal Self-Assembly of Block Alternating Copolymers via Simulation. J. Phys. Chem. B 123, 8333–8340.

Lolli, M.L., Carnovale, I.M., Pippione, A.C., Wahlgren, W.Y., Bonanni, D., Marini, E., Zonari, D., Gallicchio, M., Boscaro, V., Goyal, P., Friemann, R., Rolando, B., Bagnati, R., Adinolfi, S., Oliaro-Bosso, S., Boschi, D., 2019. Bioisosteres of Indomethacin as Inhibitors of Aldo-Keto Reductase 1C3. ACS Med. Chem. Lett. 10, 437–443.

Martinez-Colon, G.J., Moore, B.B., 2018. Prostaglandin E2 as a Regulator of Immunity to Pathogens. Pharmacol. Ther. 185, 135–146.

Mitin, T., Hunt, D., Shipley, W.U., Kaufman, D.S., Uzzo, R., Wu, C.-L., Buyyounouski, M. K., Sandler, H., Zietman, A.L., 2013. Transurethral surgery and twice-daily radiation plus paclitaxel-cisplatin or fluorouracil-cisplatin with selective bladder preservation and adjuvant chemotherapy for patients with muscle invasive bladder cancer (RTOG 0233): a randomised multicentre phase 2 trial. Lancet Oncol. 14, 863–872.

Nam, S.H., Jang, J., Cheon, D.H., Chong, S.E., Ahn, J.H., Hyun, S., Yu, J., Lee, Y., 2020. pH-Activatable cell penetrating peptide dimers for potent delivery of anticancer drug to triple-negative breast cancer. J. Control. Release. https://doi.org/10.1016/j.jconrel.2020.10.063.

Namgung, R., Mi Lee, Y., Kim, J., Jang, Y., Lee, B.H., Kim, I.S., Sokkar, P., Rhee, Y.M., Hoffman, A.S., Kim, W.J., 2014. Poly-cyclodextrin and poly-paclitaxel nano-assembly for anticancer therapy. Nat. Commun. 5, 3702.

Nguyen, H.N., Noss, E.H., Mizoguchi, F., Huppertz, C., Wei, K.S., Watts, G.F.M., Brenner, M.B., 2017. Autocrine Loop Involving IL-6 Family Member LIF, LIF Receptor, and STAT4 Drives Sustained Fibroblast Production of Inflammatory Mediators. Immunity 46, 220–232.

Nie, S., Zhang, X., Gref, R., Couvreur, P., Qian, Y., Zhang, L., 2015. Multilamellar Nanoparticles Self-Assembled from Opposite Charged Blends: Insights from Mesoscopic Simulation. J. Phys. Chem. C 119, 20649–20661.

NSCLC Meta-analysis Collaborative Group, 2014. Preoperative chemotherapy for non-small-cell lung cancer: a systematic review and meta-analysis of individual participant data. Lancet 383, 1561–1571.

Ou, W., Byeon, J.H., Thapa, R.K., Ku, S.K., Yong, C.S., Kim, J.O., 2018. Plug-and-Play Nanorization of Coarse Black Phosphorus for Targeted Chemo-photoimmunotherapy of Colorectal Cancer. ACS Nano 12, 10061–10074.

Palucka, A.K., Coussens, L.M., 2016. The Basis of Oncoimmunology. Cell 164, 1233–1247.

Ran, S., 2015. The Role of TLR4 in Chemotherapy-Driven Metastasis. Cancer Res. 75, 2405–2410.

Robey, R.W., Pluchino, K.M., Hall, M.D., Fojo, A.T., Bates, S.E., Gottesman, M.M., 2018. Revisiting the role of ABC transporters in multidrug-resistant cancer. Nat. Rev. Cancer 18, 452–464.

Rolland, N., Mehandzhiyski, A.Y., Garg, M., Linares, M., Zozoulenko, I.V., 2020. New Patchy Particle Model with Anisotropic Patches for Molecular Dynamics Simulations: Application to a Coarse-Grained Model of Cellulose Nanocrystal. J. Chem. Theory Comput. 16, 3699–3711.

Shalapour, S., Karin, M., 2019. Pas de Deux: Control of Anti-tumor Immunity by Cancer-Associated Inflammation. Immunity 51, 15–26.

Shao, Q., Wong, K.M., Seroski, D.T., Wang, Y., Liu, R., Paravastu, A.K., Hudalla, G.A., Hall, C.K., 2020. Anatomy of a selectively coassembled beta-sheet peptide nanofiber. Proc. Natl. Acad. Sci. USA 117, 4710–4717.

Shen, G., Xing, R., Zhang, N., Chen, C., Ma, G., Yan, X., 2016. Interfacial Cohesion and Assembly of Bioadhesive Molecules for Design of Long-Term Stable Hydrophobic Nanodrugs toward Effective Anticancer Therapy. ACS Nano 10, 5720–5729.

Siegel, R.L., Miller, K.D., Jemal, A., 2020. Cancer statistics, 2020. CA Cancer J. Clin. 70, 7–30.

Stefan, S.M., Wiese, M., 2019. Small-molecule inhibitors of multidrug resistance-associated protein 1 and related processes: A historic approach and recent advances. Med. Res. Rev. 39, 176–264.

Sun, H., Zhong, Z., 2020. 100th Anniversary of Macromolecular Science Viewpoint: Biological Stimuli-Sensitive Polymer Prodrugs and Nanoparticles for Tumor-Specific Drug Delivery. ACS Macro Lett. 9, 1292–1302.

Szakacs, G., Hall, M.D., Gottesman, M.M., Boumendjel, A., Kachadourian, R., Day, B.J., Baubichon-Cortay, H., Di Pietro, A., 2014. Targeting the Achilles heel of multidrug-resistant cancer by exploiting the fitness cost of resistance. Chem. Rev. 114, 5753–5774.

Tavakkoli, K.G.A., Nicaise, S.M., Gadelrab, K.R., Alexander-Katz, A., Ross, C.A., Berggren, K.K., 2016. Multilayer block copolymer meshes by orthogonal self-assembly. Nat. Commun. 7, 10518.

Teh, D.B.L., Bansal, A., Chai, C., Toh, T.B., Tucker, R.A.J., Gammad, G.G.L., Yeo, Y., Lei, Z., Zheng, X., Yang, F., Ho, J.S., Bolem, N., Wu, B.C., Gnanasammandhan, M.K., Hooi, L., Dawe, G.S., Libedinsky, C., Ong, W.Y., Halliwell, B., Chow, E.K., Lim, K.L.,

Zhang, Y., Kennedy, B.K., 2020. A Flexi-PEGDA Upconversion Implant for Wireless Brain Photodynamic Therapy. Adv. Mater. 32, e2001459.
Tolaney, S.M., Barry, W.T., Dang, C.T., Yardley, D.A., Moy, B., Marcom, P.K., Albain, K. S., Rugo, H.S., Ellis, M., Shapira, I., Wolff, A.C., Carey, L.A., Overmoyer, B.A., Partridge, A.H., Guo, H., Hudis, C.A., Krop, I.E., Burstein, H.J., Winer, E.P., 2015. Adjuvant Paclitaxel and Trastuzumab for Node-Negative, HER2-Positive Breast Cancer. N. Engl. J. Med. 372, 134–141.
Vaidyanathan, A., Sawers, L., Gannon, A.L., Chakravarty, P., Scott, A.L., Bray, S.E., Ferguson, M.J., Smith, G., 2016. ABCB1 (MDR1) induction defines a common resistance mechanism in paclitaxel- and olaparib-resistant ovarian cancer cells. Br. J. Cancer 115, 431–441.
Volk-Draper, L., Hall, K., Griggs, C., Rajput, S., Kohio, P., DeNardo, D., Ran, S., 2014. Paclitaxel therapy promotes breast cancer metastasis in a TLR4-dependent manner. Cancer Res. 74, 5421–5434.
Wang, A., Yang, Y., Qi, Y., Qi, W., Fei, J., Ma, H., Zhao, J., Cui, W., Li, J., 2016. Fabrication of Mesoporous Silica Nanoparticle with Well-Defined Multicompartment Structure as Efficient Drug Carrier for Cancer Therapy in Vitro and in Vivo. ACS Appl. Mater. Interfaces 8, 8900–8907.
Wang, D., Yu, C., Xu, L., Shi, L., Tong, G., Wu, J., Liu, H., Yan, D., Zhu, X., 2018. Nucleoside Analogue-Based Supramolecular Nanodrugs Driven by Molecular Recognition for Synergistic Cancer Therapy. J. Am. Chem. Soc. 140, 8797–8806.
Wang, X., Cheng, X., He, L., Zeng, X., Zheng, Y., Tang, R., 2019a. Self-Assembled Indomethacin Dimer Nanoparticles Loaded with Doxorubicin for Combination Therapy in Resistant Breast Cancer. ACS Appl. Mater. Interfaces 11, 28597–28609.
Wang, Y., Wu, Y., Li, K., Shen, S., Liu, Z., Wu, D., 2019b. Ultralong Circulating Lollipop-Like Nanoparticles Assembled with Gossypol, Doxorubicin, and Polydopamine via π-π Stacking for Synergistic Tumor Therapy. Adv. Funct. Mater. 29, 1805582.
Wu, Z., Beltran-Villegas, D.J., Jayaraman, A., 2020. Development of a New Coarse-Grained Model to Simulate Assembly of Cellulose Chains Due to Hydrogen Bonding. J. Chem. Theory Comput. 16, 4599–4614.
Xing, R., Zou, Q., Yuan, C., Zhao, L., Chang, R., Yan, X., 2019. Self-Assembling Endogenous Biliverdin as a Versatile Near-Infrared Photothermal Nanoagent for Cancer Theranostics. Adv. Mater. e1900822.
Xiong, H., Wang, Z., Wang, C., Yao, J., 2020. Transforming Complexity to Simplicity: Protein-Like Nanotransformer for Improving Tumor Drug Delivery Programmatically. Nano Lett. 20, 1781–1790.
Xu, C., Yang, S., Jiang, Z., Zhou, J., Yao, J., 2020. Self-Propelled Gemini-like LMWH-Scaffold Nanodrugs for Overall Tumor Microenvironment Manipulation via Macrophage Reprogramming and Vessel Normalization. Nano Lett. 20, 372–383.
Xue, P., Liu, D., Wang, J., Zhang, N., Zhou, J., Li, L., Guo, W., Sun, M., Han, X., Wang, Y., 2016. Redox-Sensitive Citronellol-Cabazitaxel Conjugate: Maintained in Vitro Cytotoxicity and Self-Assembled as Multifunctional Nanomedicine. Bioconjug. Chem. 27, 1360–1372.
Yang, H., Wang, Q., Li, Z., Li, F., Wu, D., Fan, M., Zheng, A., Huang, B., Gan, L., Zhao, Y., Yang, X., 2018. Hydrophobicity-Adaptive Nanogels for Programmed Anticancer Drug Delivery. Nano Lett. 18, 7909–7918.
Yardley, D.A., 2013. nab-Paclitaxel mechanisms of action and delivery. J. Control. Release 170, 365–372.
Zeng, X., Cheng, X., Zheng, Y., Yan, G., Wang, X., Wang, J., Tang, R., 2020. Indomethacin-grafted and pH-sensitive dextran micelles for overcoming inflammation-mediated multidrug resistance in breast cancer. Carbohydr. Polym. 237, 116139.
Zhang, C., Long, L., Xiong, Y., Wang, C., Peng, C., Yuan, Y., Liu, Z., Lin, Y., Jia, Y., Zhou, X., Li, X., 2019. Facile Engineering of Indomethacin-Induced Paclitaxel Nanocrystal Aggregates as Carrier-Free Nanomedicine with Improved Synergetic Antitumor Activity. ACS Appl. Mater. Interfaces 11, 9872–9883.
Zhang, M., Huang, Y., Hao, D., Ji, Y., Ouyang, D., 2020a. Solvation structure and molecular interactions of ibuprofen with ethanol and water: A theoretical study. Fluid Phase Equilib. 510, 112454.
Zhang, X., Li, N., Zhang, S., Sun, B., Chen, Q., He, Z., Luo, C., Sun, J., 2020b. Emerging carrier-free nanosystems based on molecular self-assembly of pure drugs for cancer therapy. Med. Res. Rev. 40, 1754–1775.
Zhang, Z., Ji, Y., 2019. Mesoporous Manganese Dioxide Coated Gold Nanorods as a Multiresponsive Nanoplatform for Drug Delivery. Ind. Eng. Chem. Res. 58, 2991–2999.
Zhang, Z., Ji, Y., 2020. Nanostructured manganese dioxide for anticancer applications: preparation, diagnosis, and therapy. Nanoscale 12, 17982–18003.
Zhen, X., Xie, C., Jiang, Y., Ai, X., Xing, B., Pu, K., 2018. Semiconducting Photothermal Nanoagonist for Remote-Controlled Specific Cancer Therapy. Nano Lett. 18, 1498–1505.
Zheng, M., Liu, Y., Wang, Y., Zhang, D., Zou, Y., Ruan, W., Yin, J., Tao, W., Park, J.B., Shi, B., 2019. ROS-Responsive Polymeric siRNA Nanomedicine Stabilized by Triple Interactions for the Robust Glioblastoma Combinational RNAi Therapy. Adv. Mater. 31, e1903277.